C. R. Physique 11 (2010) 285–292

Contents lists available at ScienceDirect

Comptes Rendus Physique

www.sciencedirect.com

Computational metallurgy and changes of scale / Métallurgie numérique et changements d'échelle

Multiscale modelling of indentation in FCC metals: From atomic to continuum

Simulations multi-échelles de l'indentation de métaux CFC : De l'atome au milieu continu

Hyung-Jun Chang, Marc Fivel *, David Rodney, Marc Verdier

SIMAP, GRENOBLE INP/CNRS, 101 Rue de la Physique, BP 46, 38402 St Martin d'Hères cedex, France

ARTICLE INFO

Keywords:
Multiscale modelling
Indentation

Mots-clés :
Simulations multi-échelles
Indentation

ABSTRACT

This work presents numerical simulations of indentation at different scales. The indentation test is chosen to illustrate the multiscale approach used in most modern studies of crystalline plasticity. The multiscale approach proposed in this work consists of passing information from one model up to another model operating at an upper scale. At the atomic scale, molecular dynamics simulations give access to the shape and position of the first dislocations induced by indentation. This information is then passed to a dislocation dynamics model that can simulate dislocation organization while the loading proceeds. At the continuum level, finite element simulations are conducted within the framework of crystal plasticity. The constitutive equations used in the continuum model are informed by dedicated dislocation dynamics simulations. Finite element simulations are quantitatively compared to experimental data demonstrating that the dislocation dynamics computations are pertinent.

RÉSUMÉ

Cet article présente plusieurs simulations d'indentation à différentes échelles. L'essai d'indentation est choisi pour illustrer les démarches multiéchelles utilisées classiquement dans les études modernes de la déformation plastique des matériaux cristallins. L'approche multiéchelle proposée consiste en un chaînage de codes : les informations obtenues par un modèle sont utilisées par le modèle fonctionnant à l'échelle supérieure. A l'échelle atomique, des simulations de dynamique moléculaire déterminent la forme et la position des premières dislocations induites par l'application d'un indenteur. Ces informations sont utilisées par le code de dynamique des dislocations qui peut simuler l'organisation des dislocations lorsque le chargement se poursuit. A l'échelle des milieux continus, des simulations d'indentation sont menées par éléments finis dans le cadre de la plasticité cristalline. Les lois de comportement utilisées sont identifiées par des simulations spécifiques menées par dynamique des dislocations. Les simulations par éléments finis sont alors comparées quantitativement aux observations expérimentales démontrant ainsi la pertinence du modèle et des données introduites.

* Corresponding author.
E-mail address: Marc.Fivel@simap.grenoble-inp.fr (M. Fivel).

1631-0705/$ – see front matter
doi:10.1016/j.crhy.2010.07.007

1. Introduction to indentation

Mechanics of plastic indentation has led to a very intense research activity, both in terms of experiments and numerical modelling [1]. With the development of instrumented indentation and scanning probe microscopy, it has become a major tool used to probe local material properties. In the case of metallic single crystals, one can distinguish different regimes depending on the indenter penetration depth. The following applies typically to Cu single crystals at room temperature for which the oxide layer is neglected. In the sub-micron depth range, the load–depth curves start with an elastic regime followed by pop-in phenomena related to strain bursts [2,3]. A required condition for such plastic dynamic instabilities is that the indented volume of the crystal should be initially relatively free of structural defects such as dislocations [4]. Otherwise load–depth curves have a continuous behavior, with a power law exponent evolving towards an expected value of 2, for example, for a self similar conical geometry indenter deforming an elasto–plastic medium. However, in this regime which extends down to depths of several tens of microns, the hardness as defined by the load divided by the area of contact under load is experimentally not constant. This corresponds to the so-called indentation size effect for which the hardness increases when the indenter penetration depth decreases. In terms of defect microstructure accompanying the plastic flow in the above mentioned regimes, one can schematize the first regime by an elasto–plastic transition where plasticity is initiated by dislocation nucleation in a small volume confined by the elastic field of the indenter contact. The second regime covers broadly the expansion of plasticity at larger scales. One observes an evolution of the dislocation microstructure: tangled dislocation walls evolve towards well defined sub-grains boundaries at the borders of local crystal rotation domains. This scales with the depth of indentation [5–7].

Today, a single numerical simulation approach covering the whole scale is not yet accessible. We present here some recent work concerning both regimes. The first example will focus on dislocation nucleation and propagation corresponding to the transition between the elastic and plastic regimes in the case of [111] spherical indentation. For this study, both Molecular Dynamics (MD) and Dislocation Dynamics (DD) simulations are used. The DD simulations give the local rules needed by DD to simulate indentation for larger depths.

The second example deals with the visco-plastic regime simulated at the continuum level by the Finite Elements Method (FEM). The constitutive equations are based on dislocation theory and use dislocation densities on the different slip systems as internal variables. The coefficients in the constitutive equations can all be computed using DD simulations. [111] conical indentations are then performed. Comparisons with load–depth curves from instrumented indentation and the resulting surface displacements by Atomic Force Microscopy (AFM) validate the set of parameters used to represent the visco-plastic behavior of pure Cu single crystals.

2. Scale transition from atom to dislocation

2.1. Molecular dynamics simulations

We performed atomistic simulations of nanoindentation along a [111] direction of a FCC crystal. The methodology used here is conventional and details can be found for example in Ref. [8]. We employed an embedded atom method potential for nickel with realistically high stacking fault energy (100 mJ/m^2) [9]. The simulation cell is shown schematically in Fig. 1a. The indenter is modelled by a repulsive sphere with a radius of 120 Å. The size of the crystal is typically $224 \times 284 \times 285$ $Å^3$ containing about 1.5 million atoms. The sphere is gradually moved into the crystal in steps of 0.1 Å along a [111] direction, with the bottom atomic layer of the crystal held fixed in that direction. Periodic boundary conditions are applied along the $(\bar{1}01)$ and $(1\bar{2}1)$ sides of the cell. Between each increment, the potential energy of the cell is minimized using a Conjugate Gradient algorithm in order to obtain a succession of equilibrium states with increasing indentation depths.

2.2. Results

The force on the indenter is shown as a function of indentation depth in Fig. 1b. As expected for displacement driven loading condition, there is an initial elastic regime that ends with a sudden drop of the indenter force. The latter corresponds to the nucleation of the first dislocations in the crystal, also called pop-in event. The nucleation process is rather complex as illustrated in Fig. 2, which shows snapshots of atomic configurations at fixed indentation depth, in the course of the first energy minimization where dislocations are nucleated. After an initial elastic deformation of the cell (Fig. 2a), defects appear a few nanometers below the surface of the crystal (Fig. 2b). This structure is highly unstable and evolves into dislocation lines, visible in Fig. 2c with their stacking faults (in orange) bordered by Shockley partials (in red). The dislocations form three interstitial prismatic loops (Fig. 2d) that each consists of dislocation segments on two slip systems that share a common Burgers vector. The loops expand in the crystal and finally detach from the surface (Figs. 2e and f), after which they move away from the surface along their glide cylinder parallel to their Burgers vector. A complex network of dislocations is left near the surface beneath the indenter. Further indentation produces a more complex network from which prismatic loops are regularly emitted.

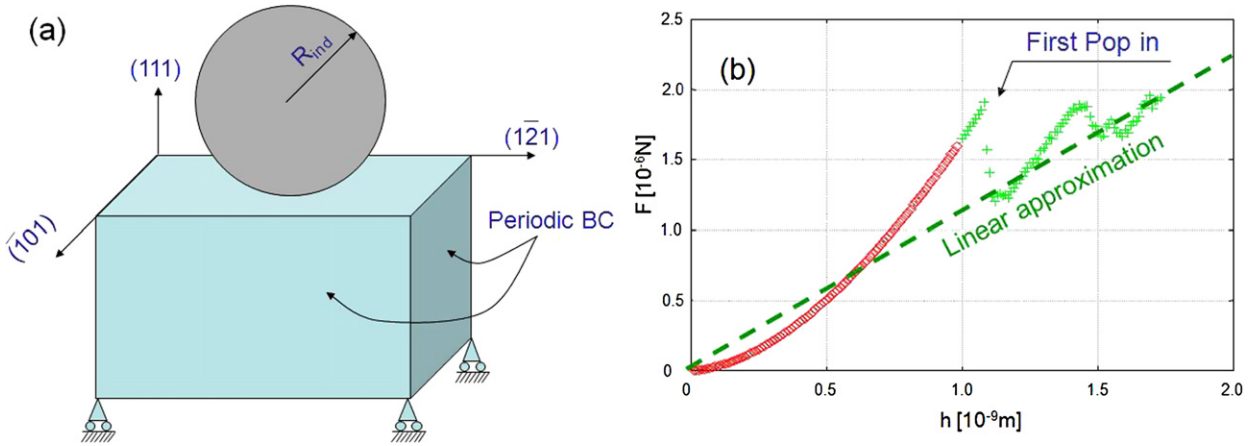

Fig. 1. (a) Schematic representation of the cell for atomistic simulations. (b) Loading curve during indentation along a [111] direction.

Fig. 1. (a) Représentation schématique de la configuration retenue pour les simulations atomiques. (b) Courbe de charge obtenue pour une indentation suivant la direction [111].

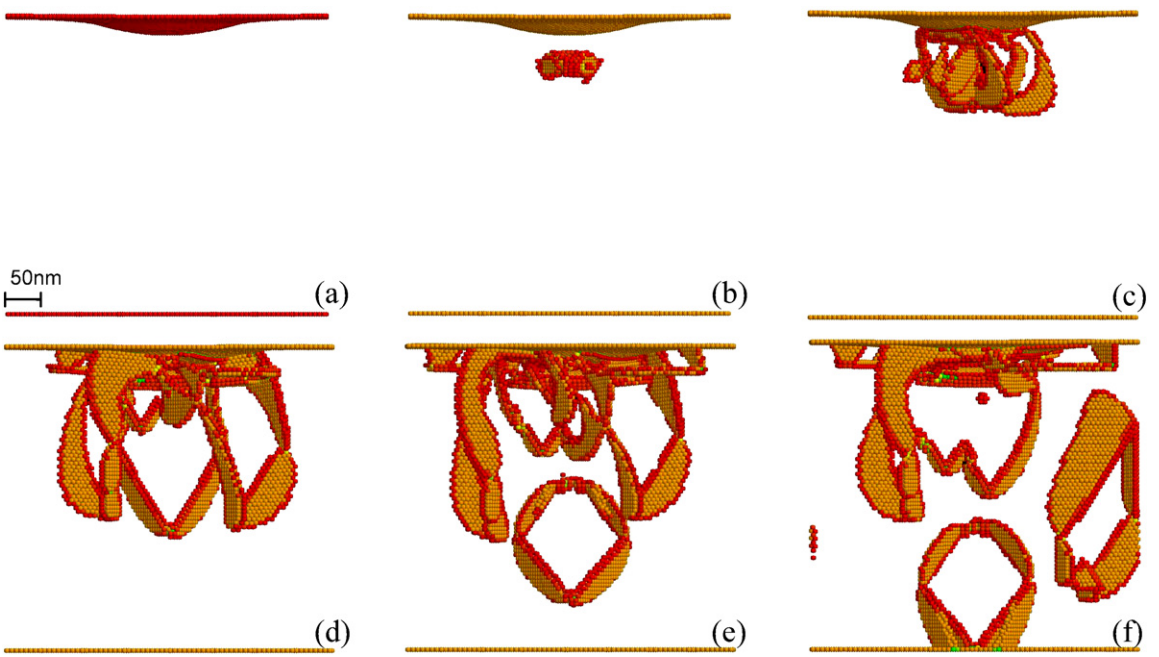

Fig. 2. Snapshots of atomic configuration during a pop-in event in the course of a [111] indentation. Are shown here only the atoms that do not have a local FCC environments (i.e. first-neighbors placed in FCC positions) (see text for details).

Fig. 2. Différentes configurations atomiques obtenues pendant un évènement de nucléation au cours d'une indentation suivant [111]. Seuls les atomes dont les atomes voisins ne sont pas en position d'un réseau cfc sont représentés (voir le texte pour plus de détails).

2.3. Transition to dislocation scale

As illustrated in Fig. 3, the atomistic simulations show that the dislocations produced by the spherical indenter are interstitial prismatic loops with the three equivalent Burgers vectors along the [111] direction. The loops being symmetrical, they plastically accommodate a net displacement along the [111] direction of indentation and the projection of their glide cylinders covers the contact area with the indenter. Once introduced in the crystal, each prismatic loop induces plastic steps on the indented surface corresponding to a punch along the loop's Burgers vector. The central triangle shared by the three nucleated loops is displaced along the [111] direction as a combination of the three displacements. In other words, the surface displacements induced by the punched-in loops constitute a rough approximation of the spherical shape of the indented surface. We will now use this information in dislocation dynamics simulations.

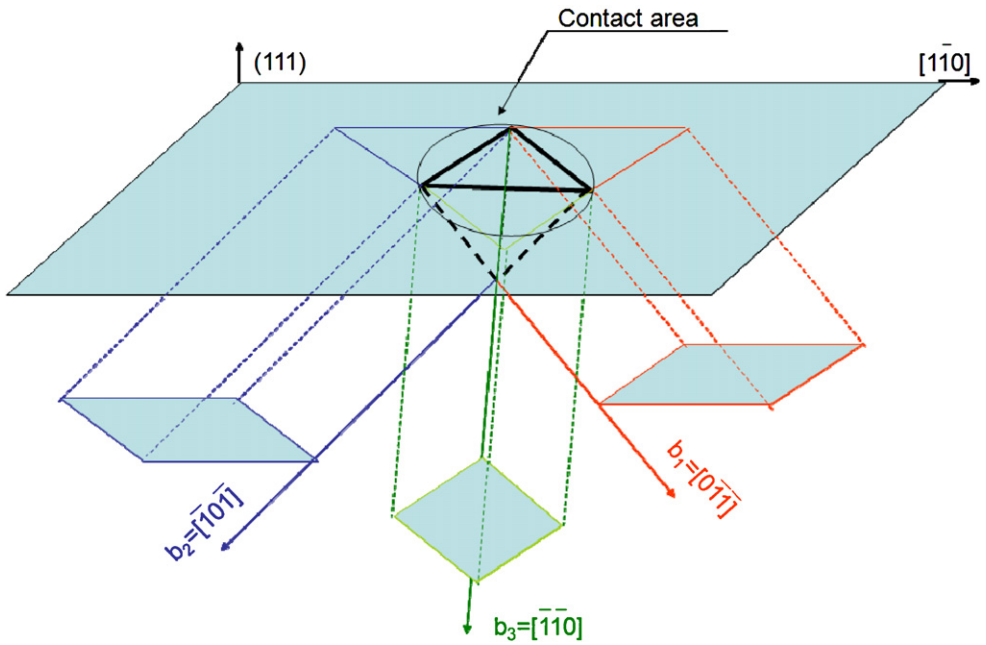

Fig. 3. Schematic description of loop nucleation process during [111] indentation.

Fig. 3. Description schématique du procédé de nucléation pour une indentation suivant [111].

2.4. Dislocation dynamics simulations

Although MD simulations can capture dislocation nucleation, the limited simulation volume precludes the observation of plastic zone expansion corresponding to indentation depth in the 0–100 nm range. This regime can, however, be investigated using DD simulations provided boundary conditions relevant to indentation loading are accounted for. This can be done using the superposition principle proposed by van der Giessen and Needleman [10]. For this purpose, the edge-screw DD code [11] is coupled to the FEM solver CAST3M [12]. As shown in Fig. 4a, the entire simulated volume is meshed with eight-node elements. The FEM computes the loading stresses which are here highly heterogeneous due to the indentation loading. Image forces induced by the top free surface are also computed by the FEM. *No specific boundary conditions are applied to the bottom and lateral surfaces.* Dislocation mobility is then given by a viscous law proportional the effective stress computed at every segmental mid-points, the effective stress being the sum of the internal stress induced by all the dislocations in the simulated volume and of the FEM stress field [11,13]. Specific contact algorithms are developed to enforce convergence of displacements under the indenter and a quasi-equilibrium state of the dislocation structure [14].

Since nucleation events cannot be predicted by DD, one has to implement this mechanism as a set of rules specifying the shape, position and number of the new dislocations loop to introduce at each time step. The former information is fully determined by the MD results as summarized in Fig. 3: three prismatic loops are introduced with radii matching the contact area. The latter is chosen in order to accommodate systematically the displacement by GND-like prismatic loops: as many loops as the number required to match the imposed displacement are introduced.

Fig. 4b shows the typical response obtained by DD simulations for a spherical [111] indentation with a tip radius of 15 nm. The green line recalls the linear approximation of the MD response as given in Fig. 1b.

After an initial elastic regime (denoted as zone I in Fig. 4b), the DD response follows the loading curve extrapolated from the MD results (stage II). During this stage, the dislocation microstructure is made of series of punched-in interstitial prismatic loops leading to triangular shape of the imprints left on the surface as shown in Fig. 5.

For larger depths, the size of the introduced prismatic loops is large enough to allow Frank–Read mechanism to operate on each arm of the loops. This leads to a spherical deformation of the surface associated to a high density of dislocations beneath the indenter. In stage III, introduction of new prismatic loops around the contact area becomes topologically difficult in the DD code due to the very high dislocation density in the lattice with the corresponding DD spatial discretization. The load–depth curve does not follow the MD prediction anymore. Plastic displacement is then achieved only by the already existing microstructure.

Hardness estimated from the ratio of the applied force to the contact area at a given depth has been computed from the DD simulations. It is found that hardness decreases with the indentation depth, which indicates that DD can reproduce the indentation size effect. Further investigations are needed to fully explain the origin of this behavior.

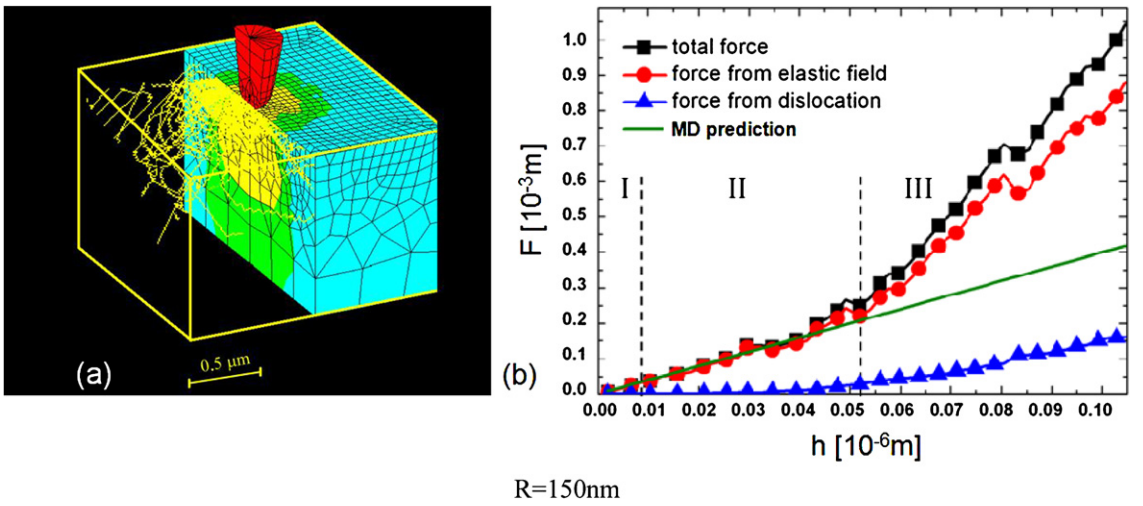

Fig. 4. DD simulations. (a) Superposition scheme coupling FE and DD simulations. (b) [111] indentation loading curves obtained by DD with a spherical tip ($R = 150$ nm).

Fig. 4. Simulations de DD. (a) Schéma de superposition couplant les EF et la DD. (b) Courbe de charge obtenues en DD avec un indenteur sphérique ($R = 150$ nm).

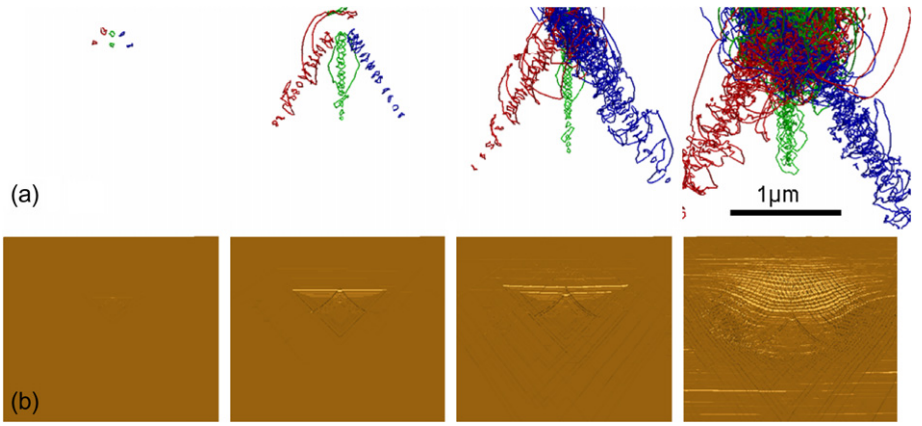

Fig. 5. DD simulations. (a) Evolution of the dislocation microstructure. (b) Surface steps induced by dislocation activity.

Fig. 5. Simulations de DD. (a) Evolution de la microstructure de dislocations. (b) Marches de surfaces imprimées par l'activité des dislocations.

3. From dislocation to continuum scale

3.1. Experimental procedure

Two different high purity (111) oriented Cu single crystals are used. The first one, $[111]_{ILL}$, was cut by spark erosion from a large crystal plate specifically grown for neutron mirror application (ILL, Institut Laue Langevin Grenoble). The second one, $[111]_{B.}$, was grown using a Bridgman process minimizing the initial dislocation density. Both crystal surfaces are carefully prepared using a Mitchell solution followed by a slow electropolishing in 80% orthophosphoric acid (0.7 V potential). The crystal quality and miscut angle are given in Table 1. $[111]_{ILL}$ and $[111]_{B.}$ crystals differ by their initial dislocation density, the lower being $[111]_{B.}$.

In Table 1, the full width at half maximum (FWHM) along the diffraction vector (θ–$2\theta°$) is proportional to the square root of the initial dislocation density and the (θ scan) indicates the existing crystal misorientation spread, i.e. the initial strain gradient (due to a slight bending of the ILL crystal). A ratio of 5 to 100 in dislocation density between the $[111]_{ILL}$ and the $[111]_{B.}$ crystals is found along with the presence of strain gradient in the ILL crystal. In other words, the ILL crystal reflects the state of a single crystal containing initial dislocations whereas crystal B is as perfect as possible.

Instrumented indentation tests are carried out to a final depth of 1.4 μm at a constant deformation rate (5×10^{-2} s^{-1}) under the continuous stiffness mode (Nanoindenter MTS-XP). Measurements reported here are made with a sapphire conical tip. The conical geometry is chosen to take into account the deformation anisotropies induced by the crystal surface

Table 1
Surface normal miscut and FWHM of (111) Bragg peaks, Cu radiation.

Tableau 1
Angles d'erreur sur la normale cristallographique, largeurs à mi-hauteur des pics de Bragg (111) en balayage (θ–2θ) et θ.

Orientation surface	Miscut		FWHM (111) (θ–2θ°)	FWHM (111) (θ scan °)
	χ (°)	θ (°)		
$^{2}[111]_{ILL}$	1.3	−0.1	0.06	0.57
$[111]_{B.}$	0.7	0.01	0.038	0.084

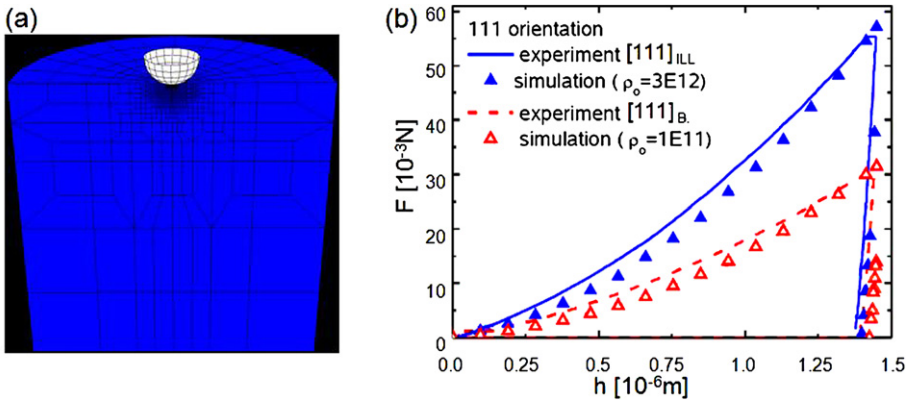

Fig. 6. FEM simulations. (a) Mesh design. (b) Loading curves obtained for different choices of the initial dislocation densities.

Fig. 6. Simulation EF. (a) Maillage. (b) Courbes de charge obtenues pour différentes valeurs de la densité initiale de dislocations.

symmetry. The final depth is large enough to avoid major effects from the tip defects and indentation size effect [15,16]. A 3D topographic recording of the tip is measured in tapping-mode AFM (Veeco 3100) and the resulting area versus height function of the tip is fitted using a sphero-conical shape function. The tip geometry is found to be approximately a cone with half angle of 71.2° terminated by a spherical tip of radius 3 µm leading to a 200 nm height of sphere like shape.

3.2. Finite element modelling

Previous works using classical FEM crystal plasticity on indentation of Cu single crystals have been published (see for example [6,17–20]), but they did not use constitutive laws based on physical parameters nor did they attempt to compare quantitatively to experiments. In this study, 3D numerical simulations are carried out using the FEM software ABAQUS [21] with a dedicated material user subroutine (VUMAT) for crystal plasticity. The simulated crystal is a cylinder of radius 100 µm meshed into 10 959 nodes and 10 308 elements along 24 sectors of 15° as shown in Fig. 6a.

The indenter is taken as rigid and has the sphero-conical shape fitted experimentally. Arbitrary Lagrangian and Eulerian (ALE) in explicit integration scheme is used and a quasi-static loading is achieved by careful monitoring the velocity of the indenter to minimize the kinetic energy at surface contact and initial unloading sequences. The imposed velocity (v) of the indenter corresponds to an equivalent strain rate $\mathrm{d}\varepsilon/\mathrm{d}t$ of 10^{-1} s^{-1} (v/h, h being the displacement) at initial contact as well as before the unloading and 1 s^{-1} in the intermediate loading regime.

Visco-plastic behavior is implemented with a physical model based on Kocks–Mecking constitutive equations of dislocation density evolution [22]. The 3D FEM implementation proposed by Tabourot et al. [23] is used. The plastic deformation tensor $\boldsymbol{\varepsilon}$ is obtained from the shear strain γ^s resolved on all {111}⟨110⟩ slip systems (1). Similarly, the resolved shear stresses τ^s are also computed from the stress tensor $\boldsymbol{\sigma}$ using Schmid tensor $\mathbf{M}^s$ through the following equations:

$$\varepsilon_{ij} = \sum_{s=1}^{12} \gamma^s M_{ij}^s \tag{1}$$

$$\tau^s = \sum_{i=1,3} \sum_{j=1,3} \sigma_{ij} M_{ij}^s \tag{2}$$

The shear strain rate is described by a classical power law taking into account the strain rate sensitivity (m) and the isotropic stress τ_μ^s:

$$\dot{\gamma}^s = \dot{\gamma}_0 \left(\frac{\tau^s}{\tau_\mu^s} \right)^{\frac{1}{m}} \operatorname{sign}(\tau^s) \tag{3}$$

Table 2
Optimized set of parameters retained to reproduce (111) indentation in Cu.

Tableau 2
Jeu de paramètres optimisé pour reproduire le comportement du cuivre indenté suivant (111).

Elasticity	C	$C_{11} = 168.4$ GPa, $C_{12} = 121.4$ GPa, $C_{44} = 75.4$ GPa
Plasticity	$\dot{\gamma}_0$	3.7×10^{-9} s^{-1}
	m	0.01
	y_c	1.43×10^{-9} (m)
	K	36
	a^{sp}	0.122, 0.122, 0.07, 0.137, 0.122, 0.625
	b	2.56×10^{-10} (m)

The hardening induced by dislocation interactions is described by Eq. (4) where ρ^p is the dislocation density on slip system p, μ is the elastic shear modulus and b is the Burgers vector magnitude. **a** is an interaction matrix specifying the average strength of interaction between dislocations on two given slip systems. Accounting for crystal symmetries, a^{sp} is only made of 6 independent terms.

$$\tau_\mu^s = \mu b \sqrt{\sum_{p=1}^{12} a^{sp} \rho^p} \tag{4}$$

Finally, the evolution of dislocation densities ρ^s on each slip system is given by Eq. (5) below

$$\dot{\rho}^s = \frac{1}{b}\left(\frac{\sqrt{\sum_{p=1}^{12} a^{sp}\rho^p}}{K} - 2y_c\rho^s\right)\left|\dot{\gamma}^s\right| \tag{5}$$

which is the core equation to describe the various stages of work-hardening rate of fcc single crystals [22]. The first term corresponds to the storage rate of dislocations: it is a ratio of the strength between the slip systems through a matrix **a**, and a semi-phenomenological scaling parameter K describing the dislocation mean free path. Recent works using DD simulation [24,25] proposed an analytical evaluation for this parameter, but in this study we use a commonly accepted reference value around 30 [13]. The second term of Eq. (5) represents the dynamic recovery rate by dislocation annihilation. y_c is the recovery length depending on the stacking fault energy [22]. Based on the physical parameters of Eq. (5), it allows one to reproduce most of fcc metals work-hardening behavior [13,23]. The set of parameters used here correspond to Cu.

In summary, the constitutive equations are all based on physical equations modelling the evolution of the dislocation densities accumulated on the different slip systems. Although Eqs. (3), (4) and (5) can all be demonstrated from physical considerations and dislocation statistics [13], the involved parameters are not easy to quantify analytically. Obviously, DD simulations can give this information. As an example, the interaction coefficient a^{sp} can be estimated thanks to series of dedicated DD simulations where the shear stress τ_μ^s needed to move a dislocation on system (s) is recorded for different values of the forest density ρ^p [13]. Recently, such dedicated simulations have led to the values of the parameters a^{sp} as collected in Table 2 [25].

FEM simulations are then performed using the continuum model. The loading curves obtained for a penetration depth up to 1.5 μm are shown in Fig. 6b. It was shown that the initial dislocation densities on each slip system have the predominant effect on the loading curve, moreover this is the only adjustable parameter once the constitutive equations are set. Thus this quantity was chosen in order to fit best the experimental data plotted as the plain lines in Fig. 6b. An initial dislocation density of $\rho_0 = 10^{11}$ m^{-2} was found for crystal $[111]_{\text{B.}}$ and a larger density of $\rho_0 = 3 \times 10^{12}$ m^{-2} for crystal $[111]_{\text{ILL}}$. This gives a dislocation ratio of 30 in good agreement with the FWHM measurements.

The shape of the surface relief is now compared to AFM observations. Results are given in Fig. 7. It appears that the profiles agree very well, both qualitatively in their shapes and quantitatively in the magnitude of the Z displacement indicated by the colors. With a higher initial density of dislocations for crystal $[111]_{\text{ILL}}$ (therefore a yield stress criterion) the plastic flow leading to 6 pile-ups is much higher (200 nm versus 50 nm height) and closer to the area of contact than crystal $[111]_{\text{B.}}$.

Complementary studies [14] have shown that the parameters in the hardening Eq. (4) and the dislocation density evolution law (5) do not affect the loading curves while they have a strong effect on the magnitude of the surface relief. This demonstrates that inverse methods to find an optimal set of parameters should not be conducted if based only on loading curves. Local information such as the actual shape of the surface relief must be taken into account.

4. Concluding remarks

The studies reported here illustrate multi-scale approaches used in crystal plasticity where information is passed along between models operating at different scales. In the case of MD–DD scale transition, the atomic simulations give the mechanism of dislocation nucleation in defect free materials. This mechanism cannot be predicted by DD simulations and thus

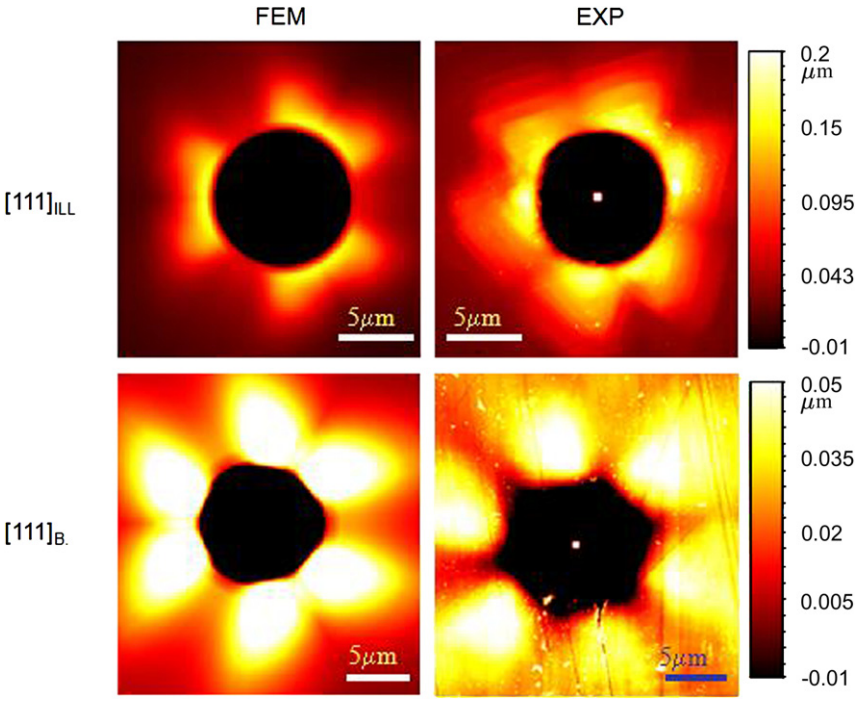

Fig. 7. Comparison of surface topography obtained for the two crystals.

Fig. 7. Comparaison du relief de surface obtenu pour les deux cristaux.

needs to be incorporated as sets of local rules. DD can then reproduce the development of plasticity during indentation for depths up to 100 nm. Since DD uses discrete elements that are precisely the carriers of plastic deformation, they involve an intrinsic length which corresponds to the Burgers vector. This explains why DD can reproduce the indentation size effect.

At the higher level, DD simulations are used to identify parameters involved in the constitutive equations of a dislocation density-based model of crystal plasticity. Such identification is impossible experimentally and only dedicated DD simulations can give a direct access to such variables. Then FEM simulations can reproduce the indentation at the real size of the actual test so that direct comparisons can be performed with experiments. It is found that the initial dislocation density can be obtained from the loading curves. On the other hand, the set of parameters used in the continuum model weakly affects the loading curve and a precise look at the actual shape of the surface imprints is needed to validate the values used.

References

[1] See for example: MRS Proceedings on Nanoindentation or J. Mater. Res. 24 (3) (2009).
[2] S. Suresh, T.G. Nieh, B.W. Choi, Scripta Mater. 41 (1999) 951–957.
[3] W.W. Gerberich, W.M. Mook, et al., J. Appl. Mech. Trans. ASME 73 (2006) 327–334.
[4] H. Bei, Y.F. Gao, S. Shim, E.P. George, G.M. Pharr, Phys. Rev. B 77 (2008) 060103.
[5] J.W. Kysar, Y.X. Gan, T.L. Morse, X. Chen, M.E. Jones, J. Mech. Phys. Sol. 55 (2007) 1554–1573.
[6] N. Zaafarani, D. Raabe, R.N. Singh, F. Roters, S. Zaefferer, Acta Mater. 54 (2006) 1863.
[7] M. Rester, C. Motz, R. Pippan, Philos. Mag. Lett. 88 (2008) 879.
[8] C.L. Kelchner, S.J. Plimpton, J.C. Hamilton, Phys. Reb. B 58 (1998) 11085.
[9] J.E. Angelo, N.R. Moody, M.I. Baskes, Modelling Simul. Mater. Sci. Eng. 3 (1995) 289.
[10] E. van der Giessen, A. Needleman, Modelling Simul. Mater. Sci. Eng. 3 (1995) 689.
[11] M. Verdier, M. Fivel, I. Groma, Modelling Simul. Mater. Sci. Eng. 6 (1998) 755.
[12] CAST3M Finite Element Method, kindly provided LMS/DMT CEA Saclay (Fr).
[13] M. Fivel, Ph.D. thesis, Institut National Polytechnique de Grenoble, 1997.
[14] H.Y. Chang, Ph.D. thesis, Grenoble Institute of Technology, 2009.
[15] K.W. McElhaney, J.J. Vlassak, W.D. Nix, J. Mater. Res. 13 (1998) 1300–1306.
[16] Y. Liu, M. Yoshino, H. Lu, R. Komanduri, Int. J. Plast. 24 (2008) 1990–2015.
[17] Y. Wang, D. Raabe, C. Kluber, F. Roters, Acta Mater. 52 (2004) 229.
[18] O. Casals, J. Ocenasek, J. Alcala, Acta Mater. 55 (2007) 55.
[19] N. Zaafarani, D. Raabe, F. Roters, S. Zaefferer, Acta Mater. 56 (2008) 31.
[20] Y. Liu, A.H.W. Ngan, Scripta Mater. 44 (2001) 237–241.
[21] ABAQUS version 6.5, Analysis User's manual, Hibbitt, Karlsson and Sorensen, Pawtucket, RI, 2004.
[22] U.F. Kocks, H. Mecking, Prog. Mater. Sci. 48 (2003) 171–273.
[23] L. Tabourot, M. Fivel, E. Rauch, Mater. Sci. Eng. A 234–236 (1997) 639.
[24] L. Kubin, B. Devincre, T. Hoc, Acta Mater. 56 (2008) 6040.
[25] B. Devincre, L. Kubin, T. Hoc, Scripta Mater. 54 (2006) 741.